

Self-organized swimming with odd elasticity

Kenta Ishimoto,^{1,*} Clément Moreau,^{1,†} and Kento Yasuda^{1,‡}

¹*Research Institute for Mathematical Sciences, Kyoto University, Kyoto 606-8502, Japan*

(Dated: September 30, 2021)

We theoretically investigated self-oscillated waves of an active solid, which have recently been introduced as a non-symmetric part of the elastic moduli, termed odd elasticity. With Purcell's three-link swimmer model, we reveal that an odd-elastic filament at a cellular scale can swim in viscous fluid via self-organized buckling instability. Also, motivated by shape fluctuation originating from internal molecular motors, we establish a general theory of microswimming under a noisy shape gait and theoretically demonstrate the odd elasticity produces biased net locomotion from random noise.

Introduction.—Swimming in a fluid is generated by interactions between elasticity and activity of a material. In particular, time-periodic wave-like beating is ubiquitous in nature, as seen from elastic filaments of cilia and flagella of microorganisms and spermatozoa [1–5] to undulatory motions of aquatic animals, including the oscillatory fins of dolphins and dinosaurs [6–9]. The self-induced traveling waves of materials can be formulated by a non-Hermitian operator from quantum to classical systems, and this breaks the Maxwell-Betti reciprocity of the material response [10–17]. For an elastic material, such self-oscillation has recently been captured by anti-symmetric components of material elastic moduli, termed as *odd elasticity*, which emerges from non-energy-conserving microscopic interactions in an active medium [18]. Material activity is, in general, generated by internal chemical reactions such as molecular machines (e.g., kinesin, dynein, and myosin) and particular enzymes [19–23], whose shapes typically fluctuate over time.

For swimming at the microscale, in particular, these non-reciprocal deformations are required for generating net locomotion to overcome the time-reversal property of the Stokes flow, or the scallop theorem [24], as theoretically formulated by the gauge field theory [25]. Microscopic propulsion is often accompanied by fluctuations from the internal motors or environmental stochasticity; however, the mechanism underlying the directed locomotion from random noise is still not fully understood [26].

The shape gait of an active material is, in general, determined as an elastohydrodynamics coupling problem, which is non-local and non-linear due to the material geometry even at low Reynolds number. Here, to investigate the elastohydrodynamics of odd-elastic material, we consider a simple but general description of a swimming filament known as Purcell's three-link swimmer model [24], which is a minimal model of microswimming with two degrees of freedom. It has been studied in various aspects of biological swimmers and artificial robots, such as efficiency, stability, and control [27–33]. Many models of elastohydrodynamic swimming necessitate internal forces that drive the

material as an input function [34–37], or further modeling on the internal structure, for example, the finer flagellar structure and regulation mechanism of molecular motors [38–41].

In contrast, our aim is to seek general features of elastohydrodynamics of an odd-elastic filament as a coarse-grained continuum description of internal activity. Hence, we will demonstrate with this simple model that an odd-elastic filament can exhibit stable swimming in viscous fluid as a self-organized elastohydrodynamic buckling instability. Further, motivated by biological fluctuations in the low-dimensional shape space, as observed in sperm and *Chlamydomonas* flagellar waveforms [42–44], we consider a noisy shape gait driven by the internal molecular fluctuations. Further, we establish a general theory in which the odd elasticity produces net locomotion from random noise through the coupling of the gauge field and probability current in the shape space.

Purcell's swimmer with odd elasticity.—The three-link model swimmer, known as Purcell's swimmer [24], consists of three slender rods of lengths ℓ_1 , ℓ_2 , and ℓ_3 connected by two hinges, as shown in Fig. 1(a), which also introduces lengthscale $L = \ell_1 + \ell_2 + \ell_3$. We denote the position of the end of the first rod as (x, y) and the angle from the x axis as θ . The relative angles at the two hinges are denoted as α_1 and α_2 . We assume the hinges are elastic [45], and linearly related to the relative angles so that the \mathbf{e}_z component of the elastic torque is given by $T_\alpha = K_{\alpha\beta}\alpha_\beta$, with Greek indices denoting the degrees of freedom for the shape, as $\alpha, \beta = \{1, 2\}$. In the elasticity matrix, \mathbf{K} , we introduce odd elasticity, in addition to the ordinary even elasticity, as [18, 26]

$$K_{\alpha\beta} = \kappa_e \delta_{\alpha\beta} + \kappa_o \epsilon_{\alpha\beta}, \quad (1)$$

where κ_e and κ_o are the even and odd elastic moduli, $\delta_{\alpha\beta}$ is the Kronecker delta, and $\epsilon_{\alpha\beta}$ is the two-dimensional anti-symmetric tensor. We will henceforth write the ratio of the two elastic moduli as $\gamma = \kappa_o/\kappa_e$. The even elastic modulus is positive and the matrix $K_{\alpha\beta}$ is positive-definite.

To show the equations of swimming dynamics, which obey the steady Stokes equations of low-Reynolds-

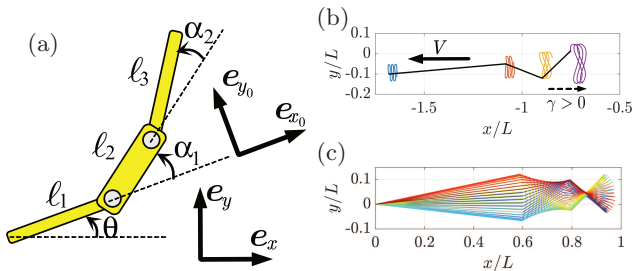


FIG. 1. (a) Schematic of Purcell's three-link swimmer. (b) An example trajectory of each end of the three rods in self-organized swimming (in the $-x$ direction) for a pusher swimmer with $\gamma > \gamma_c$. (c) Rod shape of the same swimmer as (b) superimposed with its left-most rod end being translated to the origin.

number flow, we introduce the body-fixed coordinates $\{\mathbf{e}_{x0}, \mathbf{e}_{y0}, \mathbf{e}_{z0}\}$, whose origin is located at the end of the first rod.

Using the resistive force theory and force- and torque-free condition for the swimmer, its dynamics are given in the body-fixed coordinates by

$$-\mathbf{M}(\alpha_1, \alpha_2)\dot{\mathbf{z}} = \mathbf{L}\mathbf{z}, \quad (2)$$

where $\mathbf{z} = (x_0, y_0, \theta, \alpha_1, \alpha_2)^T$ and the dot represents the time derivative. The 5×5 matrix \mathbf{M} can be taken as being symmetric, positive-definite, and dependent only on the shape parameters, α_1 and α_2 [46]. We hereafter use Roman indices for the rigid motion in the physical space such as $i, j = \{1, 2, 3\}$ to distinguish them from the Greek indices for the shape space. The matrix \mathbf{L} includes the elasticity matrix such that $L_{3+\alpha, 3+\beta} = K_{\alpha\beta}$ and the other components of \mathbf{L} are zero. From the matrix structure of the dynamics (2), the solution is formally obtained by inverting the matrix \mathbf{M} . Let us write $\mathbf{N} = \mathbf{M}^{-1}$ and we can decompose the equations into those for rigid motion and shape deformation, with $\mathbf{z}_0 = (x_0, y_0, \theta)^T$ and $\boldsymbol{\alpha} = (\alpha_1, \alpha_2)^T$, as

$$\dot{\mathbf{z}}_0 = -\mathbf{P}\mathbf{K}\boldsymbol{\alpha} \text{ and } \dot{\boldsymbol{\alpha}} = -\mathbf{Q}\mathbf{K}\boldsymbol{\alpha}, \quad (3)$$

where $P_{i\alpha} = N_{i, 3+\alpha}$ and $Q_{\alpha\beta} = N_{3+\alpha, 3+\beta}$. The second equation of (3) is closed with respect to the shape angles, whereas the first equation has an alternative form, $\dot{\mathbf{z}}_0 = \mathbf{P}\mathbf{Q}^{-1}\dot{\boldsymbol{\alpha}}$, which is not explicitly dependent on the elastic matrix and identical to the kinematic problem.

Self-organized swimming as elastohydrodynamics instability.— Numerical explorations revealed that the Purcell swimmer can swim in a self-organized manner when the swimmer shape has fore-aft asymmetry, i.e., $l_1 \neq l_3$. In Fig. 1(b), sample trajectories of the ends of the rods are shown with stable periodic shape gait [Fig. 1(c)]. With the rod lengths $l_1 > l_3 \sim l_2$ and $\gamma > 0$, the object can swim towards the left end (negative \mathbf{e}_x axis) as the beating wave travels down towards the right [Fig. 1(b)]. The right-most rod vigorously oscillates

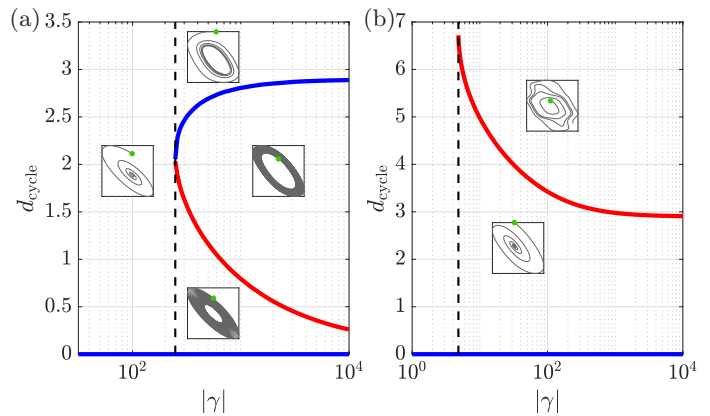


FIG. 2. Bifurcation diagrams for (a) a pusher swimmer and (b) a puller swimmer with sample trajectories in the shape space (α_1, α_2) are shown in insets. The diameter of the cycle orbit, d_{cycle} , is plotted as a function of $|\gamma|$. The equilibrium configuration is always linearly stable for a finite $|\gamma|$ for both swimmers. The pusher swimmer dynamics exhibits stable (blue) and unstable (red) limit cycles above a critical value of γ , at which a semi-stable limit cycle bifurcation occurs. For the puller swimmer, in contrast, the limit cycle is always unstable. Initial configurations are shown by a green dot in each inset.

like a *pusher* swimmer, such as sperm cells. With the reversed sign of odd viscosity ($\gamma < 0$), the swimming direction is also reversed with its oscillatory part being ahead of the longest rod, like a *puller* swimmer, such as *Leishmania* [47], but stable swimming cannot be numerically observed – though the decay to the zero equilibrium becomes extremely slow as $|\gamma|$ increases.

We then proceed to a bifurcation analysis of the elastohydrodynamic dynamical system. Around the equilibrium straight configuration, the dynamics in the shape space (3) is linearized, with $\mathbf{Q}(\boldsymbol{\alpha} = \mathbf{0})$ denoted by \mathbf{Q}_0 and $\boldsymbol{\Gamma} = \mathbf{Q}_0\mathbf{K}$, to

$$\dot{\boldsymbol{\alpha}} = -\boldsymbol{\Gamma}\boldsymbol{\alpha}, \quad (4)$$

noting that the matrix \mathbf{Q}_0 is symmetric. The eigenvalues of $\boldsymbol{\Gamma}$ are obtained as

$$\lambda = \frac{\kappa_e}{2} \left[\text{Tr}\mathbf{Q}_0 \pm \sqrt{(\text{Tr}\mathbf{Q}_0)^2 - 4(1 + \gamma^2)\det\mathbf{Q}_0} \right]. \quad (5)$$

By virtue of the positive-definiteness of the matrix, \mathbf{Q}_0 , the real part of the eigenvalues are found to be all positive, which therefore implies that the dynamics around the straight equilibrium configuration is always linearly stable [Fig. 2(a,b)].

We further analyzed the bifurcation structure and found that the system exhibits semi-stable limit cycle bifurcation at certain $\gamma = \gamma_c$ when the swimmer self-propels as a pusher [Fig. 2(a)]. In the phase space, the outer stable limit cycle contains an unstable limit cycle inside, while the origin of the phase space is a stable fixed point [Fig. 3(a)]. Even though

the equilibrium is always linearly stable, with a finite deviation, the geometrical non-linearity can sustain periodic oscillatory beating as the relaxing elastic force is being balanced by the contractile force generated through the hydrodynamic propulsion at the critical odd elasticity γ_c because the increase of γ leads to a faster traveling wave corresponding to larger propulsion. For a puller swimmer, in contrast, the propulsion force becomes extensile and thus accelerates the elastic relaxation, for which the stable limit cycle for periodic swimming cannot be realized [Fig. 2(b)]. These bifurcation structures are robustly observed in a large range of parameters [48]. When $|\gamma| \rightarrow \infty$, the time-reversal symmetry of the Stokes equations implies that the stability of a swimmer is opposite from that of a swimmer after fore-aft inversion. Hence, the swimmer with fore-aft symmetric geometry, i.e., $l_1 = l_3$, follows a closed trajectory in the shape space at this limit, while the dynamics only possess a stable fixed point at the straight configuration at a finite γ .

In addition to free swimming, we may consider different boundary conditions with one end of the rod being fixed [we set $(x, y) = (0, 0)$]. This forms ciliary propulsion rather than flagellar swimming. Both in clamped (θ fixed to 0) and hinged (unconstrained θ) boundary conditions, the semi-stable limit cycle bifurcation is realized at a certain level of $\gamma > 0$ as in the free-swimming case. Since the left end is fixed, the fore-aft asymmetry is already broken even if $l_1 = l_3$. Hence, reversing the sign of γ diminishes the periodic ciliary waveform, unlike in the free-swimming case, because it behaves as a puller.

Noisy swimming around an equilibrium.— Motivated by observations of biological swimmers [42–44], we considered swimming under a Gaussian fluctuation around the equilibrium shape, as given by

$$\dot{\alpha} = -\mathbf{\Gamma}\alpha + \xi(t). \quad (6)$$

Here, $\mathbf{\Gamma}$ is positive-definite around the equilibrium and the Gaussian noise satisfies $\langle \xi_\alpha \rangle = 0$ and $\langle \xi_\alpha(t)\xi_\beta(t') \rangle = 2D_{\alpha\beta}\delta(t-t')$, where the brackets indicate ensemble average and the diffusion matrix \mathbf{D} is symmetric and positive-definite. We assume Gaussian noise in the shape space originating from internal molecular motors and $\mathbf{D} = \kappa_n \mathbf{Q}_0$, which has the same form as the fluctuation dissipation theorem with an effective temperature [49–52]. The strength of the noise is observed to be larger by an order of magnitude than the Brownian noise at the room temperature for a sperm cell [42].

Now we rewrite the swimming dynamics using the gauge field formulation [25]. The two-dimensional rotation and linear transformation form a two-dimensional Euclidean group [53], and we represent the

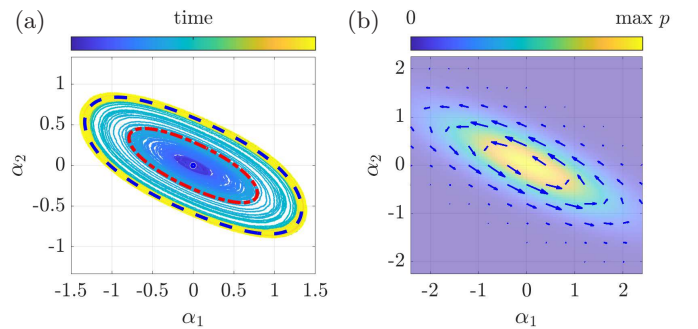


FIG. 3. (a) Trajectory in the shape space of a self-organized swimmer with noise. The time evolution is shown as a color gradation. A pusher swimmer with $\gamma < 0$ was initially at rest with a straight configuration, but once the shape exceeds the inner unstable limit cycle (red broken ellipse), it converges to the outer stable limit (blue dashed ellipse), yielding self-organized periodic swimming. See also Supplemental Movie. (b) Illustration of the steady probability distribution shown by color contour and the probabilistic current vector in the shape space depicted by arrows.

rigid motion and its generator as

$$\mathcal{R} = \begin{pmatrix} \cos \theta & \sin \theta & x \\ -\sin \theta & \cos \theta & y \\ 0 & 0 & 1 \end{pmatrix} \text{ and } \mathcal{A} = \begin{pmatrix} 0 & \dot{\theta} & \dot{x}_0 \\ -\dot{\theta} & 0 & \dot{y}_0 \\ 0 & 0 & 0 \end{pmatrix}, \quad (7)$$

which satisfy $\dot{\mathcal{R}} = \mathcal{R}\mathcal{A}$. The shape in the reference frame, $\mathcal{S}(t)$, is obtained from a rotation of that in the body-fixed frame, $\mathcal{S}_0(t)$, because $\mathcal{S}(t) = \mathcal{R}(t)\mathcal{S}_0(t)$. Further, we rewrite $\mathcal{A} = \mathcal{A}_\alpha \dot{\alpha}_\alpha$, where the matrix $\mathcal{A}_\alpha(\alpha)$ is only dependent on the shape parameters α and corresponds to the gauge potential associated with α_α . Time integration of (7) yields the path-ordering expression of the swimming dynamics. With a small deformation, $\alpha_1, \alpha_2 \ll 1$, let us expand the gauge potential around $\alpha = \mathbf{0}$ up to the quadratic term. If the deformation is periodic in time, the average swimming velocity is written [25, 28] as

$$\bar{\mathcal{A}} = \frac{1}{2} \mathcal{F}_{\alpha\beta} \overline{\alpha_\alpha \dot{\alpha}_\beta}, \quad (8)$$

where the bar indicates time average and $\mathcal{F}_{\alpha\beta} = \partial_\alpha \mathcal{A}_\beta - \partial_\beta \mathcal{A}_\alpha - [\mathcal{A}_\alpha, \mathcal{A}_\beta]$ is called the curvature tensor of the gauge field or field strength. We use the notation $\partial_\beta := \partial/\partial\alpha_\beta$ and the brackets denote the commutator, $[\mathcal{A}_\alpha, \mathcal{A}_\beta] := \mathcal{A}_\alpha \mathcal{A}_\beta - \mathcal{A}_\beta \mathcal{A}_\alpha$. The gauge field and its strength can also be represented as a third-rank tensor $[\mathcal{A}_\alpha]_{ij} = A_{ij\alpha}$ and a fourth-order tensor $[\mathcal{F}_{\alpha\beta}]_{ij} = F_{ij\alpha\beta}$, respectively.

We then seek to find the average swimming velocity, $\langle \mathcal{A} \rangle$, considering the probability distribution function in the shape space $p(\alpha, t)$ that obeys the Fokker-Planck equation associated with (6), i.e., $\partial_t p + \partial_\alpha j_\alpha = 0$ with $\partial_t = \partial/\partial t$ and the probability flux j_α , given by $j_\alpha =$

$-\Gamma_{\alpha\beta}(\alpha_\beta p) - D_{\alpha\beta}(\partial_\beta p)$. At the steady distribution, the probability flux draws closed loops [Fig. 3(d)], for which we can expect net locomotion will be produced in an averaged manner [26]. Plugging (6) into (8), the average gauge field becomes $\langle \mathcal{A} \rangle = \mathcal{F}_{\alpha\beta} \langle -\Gamma_{\beta\gamma} \alpha_\gamma \alpha_\alpha + \alpha_\alpha \xi_\beta \rangle$. With the relation $\langle \alpha_\alpha \xi_\beta \rangle = D_{\alpha\beta}$ and shape covariance matrix defined as $C_{\alpha\beta} = \langle \alpha_\alpha \alpha_\beta \rangle$, we can derive the average swimming velocity around the equilibrium by introducing a matrix $\mathbf{J} = \frac{1}{2}(\mathbf{D} - \mathbf{\Gamma C})$ in the form [54]

$$\langle \mathcal{A} \rangle = \text{Tr}(\mathcal{F}\mathbf{J}), \quad (9)$$

where the trace is taken over the shape components, i.e., $\langle A_{ij} \rangle = F_{ij\alpha\beta} J_{\beta\alpha}$. This formula (9) is a generalization of the deterministic swimming dynamics (8), and the matrix \mathbf{J} , which is proven to be anti-symmetric by plugging it into the Lyapunov equation, can be physically interpreted as the areal velocity of the probabilistic current in the shape space.

Purcell's swimmer under shape fluctuation.— With straightforward calculations, we can obtain the gauge field strength around the equilibrium, and find that only the components $F_{1312} = -F_{1321}$ are nonzero and the other components are zero. Thus, only swimming along the x -axis is possible, if a time-periodic deformation is considered. Let us denote the nonzero components as $F_{13\alpha\beta} = F\epsilon_{\alpha\beta}$, which is given by

$$F = -\ell_1 \ell_2 \ell_3 (\ell_1^2 + \ell_2^2 + \ell_1 \ell_2 + \ell_2 \ell_3 + \ell_3 \ell_1) L^{-4}. \quad (10)$$

This form is in agreement with the one found in previous studies of Purcell's swimmer [27, 55].

Because the shape space is two-dimensional, the shape covariance, which is the solution to the Lyapunov equation [56], may be solved as

$$\mathbf{C} = \frac{1}{\text{Tr}\mathbf{\Gamma}} \left[\mathbf{D} + (\det\mathbf{\Gamma})\mathbf{\Gamma}^{-1}\mathbf{D}(\mathbf{\Gamma}^T)^{-1} \right]. \quad (11)$$

Because \mathbf{J} is anti-symmetric when written as $J_{\alpha\beta} = J\epsilon_{\alpha\beta}$, we have

$$J = -\frac{3L^6\gamma}{2\tau_n} \left[(\ell_1^3 + \ell_3^3)\ell_2^3 + 3\ell_1\ell_3(\ell_1^2 + \ell_3^2)\ell_2^2 + 3\ell_1^2\ell_3^2(\ell_1 + \ell_3)\ell_2 + 2\ell_1^3\ell_3^3 \right]^{-1}, \quad (12)$$

where we introduce viscosity drag coefficient $\eta_{\parallel} = 2\pi\mu/\ln(2L/b)$, with μ and b being the medium viscosity constant and the radius of the rod, respectively. We have also assumed that the drag ratio between the perpendicular and parallel components is anisotropic, $\eta_{\perp} = 2\eta_{\parallel}$, and introduced a noise relaxation timescale, $\tau_n = \eta_{\parallel}L^3/\kappa_n$. The final expression of the average swimming velocity only possesses an e_x component, denoted by V_x , and we obtain $V_x = -2FJ$, which is linearly proportional to γ and the noise strength κ_n . In

the case of three rods with equal lengths, $\ell_1 = \ell_2 = \ell_3 = \ell$, the results are simply given by

$$F = -\frac{5\ell}{81}, \quad J = -\frac{81\gamma}{16\tau_n}, \quad \text{and} \quad V_x = -\frac{5\gamma\ell}{8\tau_n}. \quad (13)$$

The angle diffusion of the swimmer is obtained by calculating the squared angle displacement $\langle \theta^2 \rangle$, which we can estimate as $\theta = \int_0^t A_{12\alpha} \dot{\alpha}_\alpha dt' = A_{12\alpha} \alpha_\alpha + \text{h.o.t}$ for a small deformation, and it then follows that $\langle \theta^2 \rangle \approx A_{12\alpha} C_{\alpha\beta} A_{12\beta} = o(t)$, indicating that the angle diffusion from the shape fluctuation is negligible. In turn, if we further add thermal fluctuations, the odd-elastic swimmer can be represented as an active rotational Brownian particle with swimming velocity given by (9), and angle diffusion from the thermal noise.

With a large fluctuation of κ_n , a pusher filament can reach a stable limit cycle in a self-organized manner as demonstrated in Fig. 3(c), in which the swimmer is initially located at rest with a straight configuration, but once the shape exceeds the inner unstable limit cycle, it approaches the outer stable limit and exhibits self-organized periodic swimming (see Supplemental Movie).

General elastohydrodynamics.— By representing the force and torque balance equations via general degrees of freedom and their conjugate hydrodynamic force [57], we show that the symmetric resistance matrix and the symbolic elastohydrodynamic equations, (2) and (3), can be extended to a general odd-elastic material. Moreover, formula (9) notably holds for any dimensions of shape space as well as of physical space; hence, the results presented in this study, while mainly implemented for the Purcell's swimmer here, are remarkably generalizable to a wide class of low-Reynolds-number elastohydrodynamics.

We can also formally demonstrate a general odd-elastic microswimmer around an equilibrium where the non-zero noise-induced swimming velocity originates from odd elasticity, because the condition $\mathbf{J} = \mathbf{0}$ violates the detailed balance relation [56]; conversely \mathbf{J} cannot vanish if $\mathbf{\Gamma}$ has non-zero anti-symmetric components. In the odd elastic model with $\mathbf{\Gamma} = \mathbf{Q}_0\mathbf{K}$, the detailed balance was broken directly by the odd elasticity. The entropy production rate [56] is $\langle \dot{\sigma} \rangle = -\kappa_n \text{Tr}(\mathbf{\Gamma}\mathbf{G})$ with the gain matrix $\mathbf{G} = \mathbf{\Gamma C D}^{-1} - \mathbf{I} = 2\mathbf{J D}^{-1}$, so we obtain $\langle \dot{\sigma} \rangle = 2\text{Tr}(\mathbf{K}\mathbf{J}) = -4\kappa_o J > 0$ and find that the odd part of the elasticity contributes to the entropy production and that the entropy production coincides with the average power obtained by the elasticity $\langle \dot{W} \rangle = -K_{\alpha\beta} \langle \dot{\alpha}_\alpha \alpha_\beta \rangle$.

Conclusions.— The theoretical framework established in this study is applicable to a general swimmer with large degrees of freedom, such as flagella and cilia. More generally, many biological molecules function depending on their shape, as seen in molecular machines and particular enzymes accompanied with shape change under fluctuations [19–23]. Since the continuum description with odd-elasticity coarse grains relies on sub-scale active mechanisms, the current

study provides general features of the microscopic noisy elasto-hydrodynamics and therefore will be useful in modeling, understanding, and designing biological and artificial active materials.

Acknowledgments.— K.I. acknowledges the Japan Society for the Promotion of Science (JSPS), KAKENHI for Young Researchers (Grant No. 18K13456) and the Japan Science and Technology Agency, PRESTO Grant (No. JPMJPR1921). C.M. is a JSPS International Research Fellow (PE20021). K.Y. acknowledges support by a Grant-in-Aid for JSPS Fellows (Grant No. 21J00096) from the JSPS. K.I., C.M., and K.Y. were partially supported by the Research Institute for Mathematical Sciences, an International Joint Usage/Research Center located at Kyoto University.

* ishimoto@kurims.kyoto-u.ac.jp

† cmoreau@kurims.kyoto-u.ac.jp

‡ yasudak@kurims.kyoto-u.ac.jp

- [1] K. Y. Wan, Coordination of eukaryotic cilia and flagella, *Essays in Biochemistry* **62**, 829 (2018).
- [2] Y. Man, F. Ling, and E. Kanso, Cilia oscillations, *Philosophical Transactions of the Royal Society B* **375**, 20190157 (2020).
- [3] E. Lauga, *The fluid dynamics of cell motility*, Vol. 62 (Cambridge University Press, 2020).
- [4] M. F. Velho Rodrigues, M. Lisicki, and E. Lauga, The bank of swimming organisms at the micron scale (BOSO-Micro), *PloS ONE* **16**, e0252291 (2021).
- [5] E. A. Gaffney, K. Ishimoto, and B. J. Walker, Modelling motility: the mathematics of spermatozoa, *Frontiers in Cell and Developmental Biology* **9** (2021).
- [6] M. Gazzola, M. Argentina, and L. Mahadevan, Gait and speed selection in slender inertial swimmers, *Proceedings of the National Academy of Sciences* **112**, 3874 (2015).
- [7] A. J. Smits, Undulatory and oscillatory swimming, *Journal of Fluid Mechanics* **874** (2019).
- [8] N. Ibrahim, S. Maganuco, C. Dal Sasso, M. Fabbri, M. Auditore, G. Bindellini, D. M. Martill, S. Zouhri, D. A. Mattarelli, D. M. Unwin, *et al.*, Tail-propelled aquatic locomotion in a theropod dinosaur, *Nature* **581**, 67 (2020).
- [9] S. Heydari and E. Kanso, School cohesion, speed and efficiency are modulated by the swimmers flapping motion, *Journal of Fluid Mechanics* **922** (2021).
- [10] Y. Ashida, Z. Gong, and M. Ueda, Non-Hermitian physics, *Advances in Physics* **69**, 249 (2020).
- [11] S. Shankar, A. Souslov, M. J. Bowick, M. C. Marchetti, and V. Vitelli, Topological active matter, arXiv preprint arXiv:2010.00364 (2020).
- [12] C. Scheibner, W. T. Irvine, and V. Vitelli, Non-hermitian band topology and skin modes in active elastic media, *Physical Review Letters* **125**, 118001 (2020).
- [13] E. J. Bergholtz, J. C. Budich, and F. K. Kunst, Exceptional topology of non-hermitian systems, *Reviews of Modern Physics* **93**, 015005 (2021).
- [14] M. Brandenbourger, X. Locsin, E. Lerner, and C. Coulais, Non-reciprocal robotic metamaterials, *Nature communications* **10**, 1 (2019).
- [15] D. Zhou and J. Zhang, Non-hermitian topological metamaterials with odd elasticity, *Physical Review Research* **2**, 023173 (2020).
- [16] M. Fruchart, R. Hanai, P. B. Littlewood, and V. Vitelli, Non-reciprocal phase transitions, *Nature* **592**, 363 (2021).
- [17] S. Kole, G. P. Alexander, S. Ramaswamy, and A. Maitra, Layered chiral active matter: Beyond odd elasticity, *Physical Review Letters* **126**, 248001 (2021).
- [18] C. Scheibner, A. Souslov, D. Banerjee, P. Surówka, W. T. Irvine, and V. Vitelli, Odd elasticity, *Nature Physics* **16**, 475 (2020).
- [19] T. Ariga, M. Tomishige, and D. Mizuno, Nonequilibrium energetics of molecular motor kinesin, *Physical Review Letters* **121**, 218101 (2018).
- [20] A. I. Brown and D. A. Sivak, Theory of nonequilibrium free energy transduction by molecular machines, *Chemical Reviews* **120**, 434 (2019).
- [21] M. L. Mugnai, C. Hyeon, M. Hinczewski, and D. Thirumalai, Theoretical perspectives on biological machines, *Reviews of Modern Physics* **92**, 025001 (2020).
- [22] K. Yasuda and S. Komura, Nonreciprocity of a micromachine driven by a catalytic chemical reaction, *Physical Review E* **103**, 062113 (2021).
- [23] S. Ghosh, A. Somasundar, and A. Sen, Enzymes as active matter, *Annual Review of Condensed Matter Physics* **12**, 177 (2021).
- [24] E. M. Purcell, Life at low Reynolds number, *American journal of physics* **45**, 3 (1977).
- [25] A. Shapere and F. Wilczek, Geometry of self-propulsion at low Reynolds number, *Journal of Fluid Mechanics* **198**, 557 (1989).
- [26] K. Yasuda, Y. Hosaka, I. Sou, and S. Komura, Odd microswimmer, *Journal of the Physical Society of Japan* **90**, 075001 (2021).
- [27] L. E. Becker, S. A. Koehler, and H. A. Stone, On self-propulsion of micro-machines at low Reynolds number: Purcell's three-link swimmer, *Journal of Fluid Mechanics* **490**, 15 (2003).
- [28] J. E. Avron and O. Raz, A geometric theory of swimming: Purcell's swimmer and its symmetrized cousin, *New Journal of Physics* **10**, 063016 (2008).
- [29] E. Passov and Y. Or, Dynamics of Purcell's three-link microswimmer with a passive elastic tail, *The European Physical Journal E* **35**, 1 (2012).
- [30] R. L. Hatton, Y. Ding, H. Choset, and D. I. Goldman, Geometric visualization of self-propulsion in a complex medium, *Physical Review Letters* **110**, 078101 (2013).
- [31] L. Giraldi, P. Martinon, and M. Zoppello, Optimal design of Purcell's three-link swimmer, *Physical Review E* **91**, 023012 (2015).
- [32] C. Moreau, Local controllability of a magnetized Purcell's swimmer, *IEEE Control Systems Letters* **3**, 637 (2019).
- [33] E. Zheng, M. Brandenbourger, L. Robinet, P. Schall, E. Lerner, and C. Coulais, Self-oscillation and synchronisation transitions in elasto-active structures, arXiv preprint arXiv:2106.05721 (2021).
- [34] S. D. Olson, S. Lim, and R. Cortez, Modeling the dynamics of an elastic rod with intrinsic curvature and twist using a regularized Stokes formulation, *Journal of Computational Physics* **238**, 169 (2013).
- [35] J. Simons, L. Fauci, and R. Cortez, A fully three-dimensional model of the interaction of driven elastic

- filaments in a stokes flow with applications to sperm motility, *Journal of Biomechanics* **48**, 1639 (2015).
- [36] K. Ishimoto and E. A. Gaffney, An elastohydrodynamical simulation study of filament and spermatozoan swimming driven by internal couples, *IMA Journal of Applied Mathematics* **83**, 655 (2018).
- [37] H. Gadêlha and E. A. Gaffney, Flagellar ultrastructure suppresses buckling instabilities and enables mammalian sperm navigation in high-viscosity media, *Journal of The Royal Society Interface* **16**, 20180668 (2019).
- [38] I. H. Riedel-Kruse, A. Hilfinger, J. Howard, and F. Jülicher, How molecular motors shape the flagellar beat, *HFSP Journal* **1**, 192 (2007).
- [39] A. A. Evans and E. Lauga, Propulsion by passive filaments and active flagella near boundaries, *Physical Review E* **82**, 041915 (2010).
- [40] H. Gadêlha, E. A. Gaffney, and A. Goriely, The counterbend phenomenon in flagellar axonemes and cross-linked filament bundles, *Proceedings of the National Academy of Sciences* **110**, 12180 (2013).
- [41] P. Bayly and K. Wilson, Analysis of unstable modes distinguishes mathematical models of flagellar motion, *Journal of the Royal Society Interface* **12**, 20150124 (2015).
- [42] R. Ma, G. S. Klindt, I. H. Riedel-Kruse, F. Jülicher, and B. M. Friedrich, Active phase and amplitude fluctuations of flagellar beating, *Physical Review Letters* **113**, 048101 (2014).
- [43] K. Y. Wan and R. E. Goldstein, Rhythmicity, recurrence, and recovery of flagellar beating, *Physical Review Letters* **113**, 238103 (2014).
- [44] K. Ishimoto, H. Gadêlha, E. A. Gaffney, D. J. Smith, and J. Kirkman-Brown, Coarse-graining the fluid flow around a human sperm, *Physical Review Letters* **118**, 124501 (2017).
- [45] C. Moreau, Local controllability of a magnetized Purcell's swimmer, *IEEE Control Systems Letters* **3**, 637 (2019).
- [46] See Supplemental Material for the properties of the matrix.
- [47] B. J. Walker, R. J. Wheeler, K. Ishimoto, and E. A. Gaffney, Boundary behaviours of leishmania mexicana: A hydrodynamic simulation study, *Journal of theoretical biology* **462**, 311 (2019).
- [48] Further discussions are provided in Supplemental Material.
- [49] A. Lau and T. C. Lubensky, Fluctuating hydrodynamics and microrheology of a dilute suspension of swimming bacteria, *Physical Review E* **80**, 011917 (2009).
- [50] K. I. Morozov and L. M. Pismen, Motor-driven effective temperature and viscoelastic response of active matter, *Physical Review E* **81**, 061922 (2010).
- [51] D. Loi, S. Mossa, and L. F. Cugliandolo, Effective temperature of active complex matter, *Soft Matter* **7**, 3726 (2011).
- [52] D. Levis and L. Berthier, From single-particle to collective effective temperatures in an active fluid of self-propelled particles, *EPL (Europhysics Letters)* **111**, 60006 (2015).
- [53] M. F. Lapa and T. L. Hughes, Swimming at low Reynolds number in fluids with odd, or hall, viscosity, *Physical Review E* **89**, 043019 (2014).
- [54] Further derivations and physical interpretations are provided in Supplemental Material.
- [55] L. Koens and E. Lauga, Geometric phase methods with stokes theorem for a general viscous swimmer, *Journal of Fluid Mechanics* **916** (2021).
- [56] J. B. Weiss, Fluctuation properties of steady-state langevin systems, *Physical Review E* **76**, 061128 (2007).
- [57] M. Doi, *Soft matter physics* (Oxford University Press, 2013).

Symmetric properties of the resistance matrix and the diffusion matrix

We denote the positions of ends of the rods in the body-fixed coordinates as $\mathbf{r}_0, \mathbf{r}_1, \mathbf{r}_2, \mathbf{r}_3$. From the definition of the body-fixed coordinates, $\mathbf{r}_0 = \mathbf{0}$, $\mathbf{r}_1 = \ell_1 \mathbf{e}_{x0}$, $\mathbf{r}_2 = \mathbf{r}_1 + \ell_2(\cos \alpha_1 \mathbf{e}_{x0} + \sin \alpha_1 \mathbf{e}_{y0})$, and $\mathbf{r}_3 = \mathbf{r}_2 + \ell_2(\cos(\alpha_1 + \alpha_2) \mathbf{e}_{x0} + \sin(\alpha_1 + \alpha_2) \mathbf{e}_{y0})$. From the linearity, the two-dimensional surface velocity of a Purcell swimmer in the body-fixed coordinates at the position \mathbf{r} can then be represented in matrix form, using the state vector \mathbf{z} , as

$$\mathbf{v} = \mathbf{H}\dot{\mathbf{z}}. \quad (14)$$

The entries of the matrix $\mathbf{H} = \mathbf{H}(\mathbf{r}; \mathbf{z})$ are given by

$$\mathbf{H} = \begin{pmatrix} 1 & 0 & -r_0 \sin \theta_0 & -g_1(\mathbf{r})r_1 \sin \theta_1 & -g_2(\mathbf{r})r_2 \sin \theta_2 \\ 0 & 1 & r_0 \cos \theta_0 & g_1(\mathbf{r})r_1 \cos \theta_1 & g_2(\mathbf{r})r_2 \cos \theta_2 \end{pmatrix}, \quad (15)$$

where we have introduced the lengths of vectors $r_0 = |\mathbf{r} - \mathbf{r}_0|$, $r_1 = |\mathbf{r} - \mathbf{r}_1|$, and $r_2 = |\mathbf{r} - \mathbf{r}_2|$; angles from the \mathbf{e}_{x0} axis as $\theta_0 = \arg(\mathbf{r} - \mathbf{r}_0)$, $\theta_1 = \arg(\mathbf{r} - \mathbf{r}_1)$, and $\theta_2 = \arg(\mathbf{r} - \mathbf{r}_2)$; and functions $g_1(\mathbf{r})$ and $g_2(\mathbf{r})$ as

$$g_1(\mathbf{r}) = \begin{cases} 0 & (\mathbf{r} \text{ is on the first rod}) \\ 1 & (\mathbf{r} \text{ is on the second and third rods}) \end{cases} \quad (16)$$

and

$$g_2(\mathbf{r}) = \begin{cases} 0 & (\mathbf{r} \text{ is on the first and second rods}) \\ 1 & (\mathbf{r} \text{ is on the third rod}) \end{cases}. \quad (17)$$

The surface traction force \mathbf{f} defines the conjugate hydrodynamic force vector \mathbf{h} by the integral over the swimmer surface [57]

$$\mathbf{h} = \int_S \mathbf{f}^T \mathbf{H} dS. \quad (18)$$

By direct calculation, we obtain $\mathbf{h} = (F_{x0}, F_{y0}, T_z, T_{1z}, T_{2z})^T$. Here, F_{x0} and F_{y0} are the total hydrodynamic force along the \mathbf{e}_{x0} and \mathbf{e}_{y0} axes, respectively, and T_z is the total hydrodynamic torque. T_{1z} and T_{2z} are internal torque around the points \mathbf{r}_1 and \mathbf{r}_2 , respectively, and these should be balanced by the elastic torque. If we write down the force and torque balance equations for the vector \mathbf{h} , we obtain the elastohydrodynamic equation

$$-\mathbf{M}\dot{\mathbf{z}} = \mathbf{L}\mathbf{z}, \quad (19)$$

as in the main text, where \mathbf{M} is the resistance matrix. If the resistance matrix is introduced between the generalized velocity and its conjugate force, the resistance matrix found to be symmetric and positive-definite by the Lorentz reciprocal relation [57].

Finally, we explicitly present the components of the matrix $\mathbf{D} = \kappa_n \mathbf{Q}_0$. As in the main text, we introduce

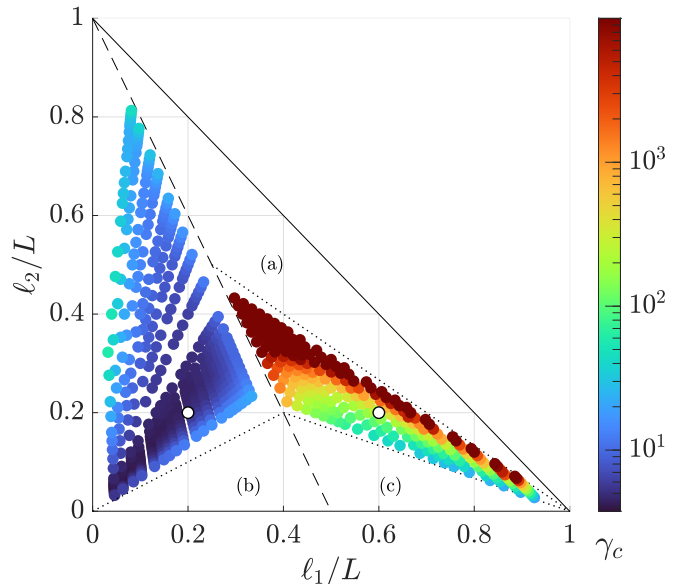


FIG. 4. Bifurcation value γ_c with respect to the ratios ℓ_1/L and ℓ_2/L . The dashed line separates the $\ell_1 < \ell_3$ region on the left (puller case) from the $\ell_1 > \ell_3$ region on the right (pusher case). In areas (a), (b), and (c), delineated by indicative dotted lines, no bifurcation can be observed. White dots represent the values used on Fig. 2 of the main text.

lengthscale $L = \ell_1 + \ell_2 + \ell_3$ and viscosity drag coefficient $\eta_{\parallel} = 2\pi\mu/\ln(2L/b)$ with μ and b being the medium viscosity constant and radius of the rod, respectively. We also assume the drag anisotropy ratio between the perpendicular and parallel components, $\eta_{\perp} = 2\eta_{\parallel}$, and noise relaxation timescale, $\tau_n = \eta_{\parallel}L^3/\kappa_n$. The expressions are then given by

$$D_{11} = \frac{6}{\tau_n} \times \frac{(\ell_1 + \ell_2)^3(\ell_1 + \ell_2 + \ell_3)^4}{\ell_1^3 \ell_2^2 (4\ell_2(\ell_1 + \ell_2 + \ell_3) + 3\ell_1 \ell_3)} \quad (20)$$

$$D_{22} = \frac{6}{\tau_n} \times \frac{(\ell_2 + \ell_3)^3(\ell_1 + \ell_2 + \ell_3)^4}{\ell_2^2 \ell_3^3 (4\ell_2(\ell_1 + \ell_2 + \ell_3) + 3\ell_1 \ell_3)} \quad (21)$$

$$D_{12} = D_{21} = -\frac{3L^3}{\tau_n} \times \left[3\ell_2^3 + 6(\ell_1 + \ell_3)\ell_2^2 + (3\ell_1^2 + 8\ell_1\ell_3 + 3\ell_3^2)\ell_2 + 2\ell_1\ell_3(\ell_1 + \ell_3) \right] / [\ell_1 \ell_2^2 \ell_3 (4\ell_2(\ell_1 + \ell_2 + \ell_3) + 3\ell_1 \ell_3)], \quad (22)$$

respectively.

Influence of the swimmer's geometry

In this section, we discuss the influence of the segment lengths ℓ_1, ℓ_2, ℓ_3 on the swimming behavior, particularly on the value γ_c at which the bifurcation displayed in Fig. 2 of the main text occurs. As above, we define the lengthscale $L = \ell_1 + \ell_2 + \ell_3$ and study the variation of γ_c with respect to the non-dimensional ratios ℓ_1/L and ℓ_2/L , as shown in Fig. 4. For positive values of γ , the

swimmer behaves as a puller (resp. pusher) if $\ell_1 < \ell_3$ (resp. $\ell_1 > \ell_3$), which coincides with the region on the left (resp. right) of the dashed line on Fig. 4. The colored dots cover the areas where a bifurcation similar to the ones presented in Fig. 2 of the main text can be observed, showing that this bifurcation phenomenon holds for a wide array of swimmer geometries. The white dots indicate the values used in Fig. 2 of the main text. Strikingly, the bifurcation occurs for much larger values of γ in the pusher case, as indicated by the colors on Fig. 4: γ_c remains less than 10^2 in the pusher case, while it ranges between 10^2 and more than 10^4 in the puller case. In regions marked (a) and (b), all the orbits converge to the stable equilibrium 0 – though the convergence speed is extremely slow. In region (c), the nonzero stable cycle observed for the puller becomes unstable, with the orbits then converging to a nonphysical stable cycle (with values of α_i greater than π).

Noisy swimmer around the equilibrium

Here, we consider an n -dimensional general swimmer with N -dimensional shape space; in particular, for the Purcell swimmer, $n = 5$ and $N = 2$. We write the generator for the n -dimensional Euclidean group \mathcal{A} , which can be represented as an $(n+1) \times (n+1)$ matrix. The swimming velocity with a small deformation can be expanded as

$$\mathcal{A}(\boldsymbol{\alpha}) = \mathcal{A}_\alpha(\mathbf{0})\dot{\alpha}_\alpha + \frac{1}{2}(\mathcal{G}_{\alpha\beta}(\mathbf{0}) + \mathcal{F}_{\alpha\beta}(\mathbf{0}))\alpha_\alpha\dot{\alpha}_\beta, \quad (23)$$

where $\mathcal{G}_{\alpha\beta}$ and $\mathcal{F}_{\alpha\beta}$ indicate the symmetric and anti-symmetric part of the second-order term, respectively, and the latter is identical to the strength of the gauge field or the curvature of the gauge field.

We consider the Langevin equation for the dynamics around the origin of the shape space, given by

$$\dot{\boldsymbol{\alpha}} = -\boldsymbol{\Gamma}\boldsymbol{\alpha} + \boldsymbol{\xi}(t), \quad (24)$$

with the zero-mean Gaussian noise $\xi_\alpha(t)$. Here, the $N \times N$ matrix $\boldsymbol{\Gamma}$ is constant in time and positive-definite, representing deterministic dynamics, which is linearly stable around the origin of the shape space. For the Purcell swimmer in the main text, $\boldsymbol{\Gamma} = \mathbf{Q}_0\mathbf{K}$.

The Gaussian noise satisfies

$$\langle \xi_\alpha(t)\xi_\beta(t') \rangle = 2D_{\alpha\beta}\delta(t-t'), \quad (25)$$

where the brackets indicate ensemble average, $\delta(t)$ is the Dirac delta function, and the diffusion matrix \mathbf{D} is symmetric and positive-definite. We assume the diffusion matrix is related to the mobility sub-matrix in the same form as the fluctuation-dissipation theorem with an effective temperature of $\mathbf{D} = \kappa_n\mathbf{Q}_0$, where κ_n is the amount of noise with a physical unit of energy

and assumed to be sufficiently larger than the room temperature $\kappa_n \gg k_B T$. In this section hereafter, we will not explicitly indicate that the evaluation point is at $\boldsymbol{\alpha} = \mathbf{0}$.

By plugging (25) into (24) and noting that the equal-time correlation between the shape and the noise can be obtained by $\langle \alpha_\alpha \xi_\beta \rangle = D_{\alpha\beta}$, the average swimming velocity becomes

$$\begin{aligned} \langle \mathcal{A} \rangle &= \frac{1}{2}(\mathcal{G}_{\alpha\beta} + \mathcal{F}_{\alpha\beta})\langle \alpha_\alpha \dot{\alpha}_\beta \rangle \\ &= -\frac{1}{2}(\mathcal{G}_{\alpha\beta} + \mathcal{F}_{\alpha\beta})(\Gamma_{\beta\gamma}C_{\gamma\alpha} - D_{\alpha\beta}), \end{aligned} \quad (26)$$

because the first-order term vanishes, $\langle \dot{\alpha}_\alpha \rangle = 0$. Here we introduced the shape covariance matrix, $C_{\alpha\beta} = \langle \alpha_\alpha \alpha_\beta \rangle$, which obeys the Lyapunov equation [56],

$$\boldsymbol{\Gamma}\mathbf{C} + \mathbf{C}\boldsymbol{\Gamma}^T = 2\mathbf{D}, \quad (27)$$

with superscript T denoting transpose of the matrix, and the formal solution may be written as

$$\mathbf{C} = 2 \int_{-\infty}^0 e^{\boldsymbol{\Gamma}t} \mathbf{D} e^{\boldsymbol{\Gamma}^T t} dt. \quad (28)$$

The time-dependent probability distribution function in the shape space $p(\boldsymbol{\alpha}, t)$ can be obtained from the Fokker-Planck equation associated with (24), i.e., $\partial p / \partial t + \partial j_\alpha / \partial \alpha_\alpha = 0$ with the probability flux j_α given by

$$j_\alpha = -p\Gamma_{\alpha\beta}\alpha_\beta - D_{\alpha\beta}\frac{\partial p}{\partial \alpha_\beta}. \quad (29)$$

The steady-state probability distribution function is the Gaussian function,

$$p(\boldsymbol{\alpha}) = \frac{1}{(2\pi)^{N/2}\sqrt{\det \mathbf{C}}} \exp\left[-\frac{1}{2}\boldsymbol{\alpha}^T \mathbf{C}^{-1} \boldsymbol{\alpha}\right], \quad (30)$$

and plugging this expression into (29) leads to the steady-state probability current, $\mathbf{j} = \boldsymbol{\Omega}\boldsymbol{\alpha}p$, where the matrix $\boldsymbol{\Omega}$ is defined as

$$\boldsymbol{\Omega} = -\boldsymbol{\Gamma} + \mathbf{D}\mathbf{C}^{-1}, \quad (31)$$

where $\boldsymbol{\Omega}$ may be interpreted as the matrix of rotational velocity of the probability current in the shape space and the vector $\boldsymbol{\Omega}\boldsymbol{\alpha}$ represents the shape space velocity. At steady state, by $\partial j_\alpha / \partial \alpha_\alpha = 0$, substituting (30) yields the traceless property of the matrix, $\text{Tr} \boldsymbol{\Omega} = 0$.

Let us write

$$\mathbf{J} = \frac{1}{2}\boldsymbol{\Omega}\mathbf{C} = \frac{1}{2}(\mathbf{D} - \boldsymbol{\Gamma}\mathbf{C}), \quad (32)$$

which may be interpreted as the areal velocity of the probability current in the shape space. By definition of \mathbf{J} , its transpose becomes $2\mathbf{J}^T = \mathbf{C}\boldsymbol{\Omega}^T = \mathbf{C}(\mathbf{C}^{-1}\mathbf{D} -$

$\mathbf{\Gamma}^T$), and from the Lyapunov equation (27), it follows that $\mathbf{J}^T = -\mathbf{J}$, from which we conclude that \mathbf{J} is anti-symmetric.

With areal velocity matrix \mathbf{J} , the average swimming velocity (26) can be finally derived,

$$\langle \mathcal{A} \rangle = \text{Tr}((\mathcal{G} + \mathcal{F})\mathbf{J}) = \text{Tr}(\mathcal{F}\mathbf{J}), \quad (33)$$

where the trace is taken over the shape indices. In the second equality, we used $\text{Tr}(\mathcal{G}\mathbf{J}) = 0$, since \mathcal{G} is symmetric and \mathbf{J} is anti-symmetric in the indices of shape space.

For simplicity, we first consider the $N = 2$ case as in the main text. We rewrite $(\mathcal{F}_{\alpha\beta})_{ij} = F_{ij\alpha\beta} = (\sqrt{\det \mathcal{F}})_{ij} \epsilon_{\alpha\beta}$ with an $(n+1) \times (n+1)$ matrix $\sqrt{\det \mathcal{F}}$, noting the determinant is taken for the shape space labels. By direct calculation, we have $\text{Tr}(\mathcal{F}\mathbf{J}) = -2\sqrt{\det \mathcal{F}}\sqrt{\det \mathbf{J}} = -2\sqrt{\det \mathcal{F}}\sqrt{\det \mathbf{C}}\sqrt{\det \mathbf{\Omega}}$. From the zero trace of $\mathbf{\Omega}$, the eigenvalues of the matrix are simply $\nu = \pm i\sqrt{\det \mathbf{\Omega}}$, which are pure imaginary. The average swimming velocity is therefore written as

$$\langle \mathcal{A} \rangle = 2\sqrt{\det \mathcal{F}}\sqrt{\det \mathbf{C}}|\nu|, \quad (34)$$

which successfully generalizes the finding in the three-sphere model [Eq. (19) of Ref. [26]]. The form in (34) shows that the average velocity is represented by the products of a shape-dependent geometrical factor, the explored area in the shape space, and the speed of rotational probability flux. The product of the latter two indicates the areal velocity.

Formula (34) is easily extended into a general shape space with N dimensions. The anti-symmetric matrix, \mathbf{J} , can be block-diagonalized by an orthogonal matrix,

$$\begin{pmatrix} \tilde{\mathbf{J}}^{(1)} & & O & O \\ & \ddots & & \vdots \\ O & & \tilde{\mathbf{J}}^{(d)} & \vdots \\ O & \dots & \dots & O \end{pmatrix}, \quad (35)$$

where the 2×2 matrices $\tilde{\mathbf{J}}^{(1)} \dots, \tilde{\mathbf{J}}^{(d)}$ are all real anti-symmetric with eigenvalues all pure imaginary, where $d = [N/2]$ is the integer part of $N/2$. With positive real numbers $\omega_1, \dots, \omega_d$, the matrices are represented as $\tilde{\mathbf{J}}_{\alpha\beta}^{(1)} = i\omega_1 \epsilon_{\alpha\beta}$. Similarly, with the same orthogonal

transformation,

$$\begin{pmatrix} \tilde{\mathcal{F}}^{(1)} & & * & * \\ & \ddots & & \vdots \\ * & & \tilde{\mathcal{F}}^{(d)} & \vdots \\ * & \dots & \dots & * \end{pmatrix}, \quad (36)$$

where asterisks denote arbitrary entries. Here, $\tilde{\mathcal{F}}^{(1)} \dots, \tilde{\mathcal{F}}^{(d)}$ are real anti-symmetric with respect to the shape indices, and we again rewrite these as $(\tilde{\mathcal{F}}^{(1)})_{\alpha\beta} = \tilde{F}_{ij\alpha\beta}^{(1)} = (\sqrt{\det \tilde{\mathcal{F}}^{(1)}})_{ij} \epsilon_{\alpha\beta}$. The average swimming velocity is then simplified in the form

$$|\langle \mathcal{A} \rangle| = \sum_{q=1}^d |\text{Tr}(\tilde{\mathcal{F}}^{(q)}\tilde{\mathbf{J}}^{(q)})| = \sum_{q=1}^d |\omega_q| \sqrt{\det \tilde{\mathcal{F}}^{(q)}}. \quad (37)$$

The average swimming velocity is decomposed into the contributions from the shape subspace and represented as the product of field strength and areal velocity in each 2D sub-space. In the case with 3D shape space ($N = 3$), the probability current lies in the 2D plane in 3D space. When $N = 4$, the dynamics in the shape space are then decomposed into two separated 2D planes.

Caption of the Supplemental Movie

A simulation movie of Purcell's swimmer undergoing shape fluctuation with the positions of the end of the left-most rod is traced over time. A pusher swimmer is considered with the model parameters $(\ell_1/L, \ell_2/L, \ell_3/L) = (0.2, 0.2, 0.6)$ and $\gamma = -300$, where $L = \ell_1 + \ell_2 + \ell_3$ is the total length of the rods. This set of parameters exhibits the same dynamics as in Fig. 1(b,c), and Fig. 2 of the main text but with opposite swimming direction. The odd-elastic swimmer was initially at rest with a straight configuration. The dynamics are separated into three phases. (1) The swimmer moves slightly towards the right with small amplitude (blue), until the shape exceeds the inner unstable limit cycle. (2) The beating wave is then amplified (orange) and reaches stable swimming (yellow).

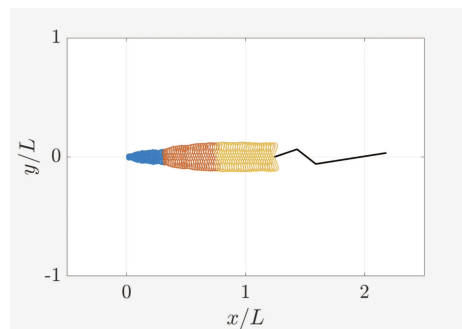


FIG. 5. Snapshot of Supplemental Movie.